Experimental evidence of reaction-induced fracturing during olivine carbonation.

Experimental evidence of reaction-induced fracturing during olivine carbonation

Wenlu Zhu[1*], Florian Fusseis[2], Harrison Lisabeth[1], Tiange Xing[1], Xianghui Xiao[3], Vincent De Andrade[3], Shun-ichiro Karato[4]

[1]Department of Geology, University of Maryland, College Park, MD 20782, USA
[2]School of Geosciences, University of Edinburgh, Edinburgh, EH9 3FE, UK
[3]Advanced Photon Source, Argonne National Laboratory, Argonne, IL 60439, USA
[4]Department of Geology and Geophysics, Yale University, New Haven, CT 06511, USA

*Correspondence to: Wenlu Zhu (wzhu@umd.edu)

Abstract. Mineral carbonation, a process that binds CO_2 in the form of carbonates by silicate weathering, is widespread on the Earth's surface. Because of the abundance of silicate rocks and the permanence of the carbonated solids, sequestering CO_2 via mineral carbonation has generated lots of interests. However, it is unclear how the fluid-rock reaction proceeds to completion in spite of an increasing solid volume. We conducted a mineral carbonation experiment in which a sintered olivine aggregate reacted with a sodium bicarbonate solution at reservoir conditions. Time-resolved synchrotron X-ray microtomographic images show cracks in polygonal patterns arising in the surface layers and propagating into the interior of the olivine aggregate. The nanotomography data reveal that the incipient cracks intersect at right angles. We infer that stretching due to non-uniform volume expansion generates polygonal cracking of the surfaces. Our data shed new lights on the processes that controls hydration and carbonation of peridotite.

Introduction

Hydration and carbonation of mantle peridotite are widespread on the surface of the Earth. Such alteration exerts controls in lithosphere strength, subduction zone geodynamics, hydrothermal circulation, water and carbon cycle. Mineral carbonation, in which CO_2 is chemically incorporated in silicate rocks to form carbonate minerals, is also recognized as a potentially safe and permanent method of CO_2 sequestration [e.g., Sefriz, 1990; Lackner, 2003] and was recently successfully tested in an industrial scale [Matter et al., 2016]. The naturally abundant mineral olivine (($Fe, Mg)_2SiO_4$), especially its magnesium end-member forsterite (Mg_2SiO_4), has been a focus of carbon mineralization research [Goff and Lackner, 1998; Giammar

30 et al., 2005; Gerdemann et al., 2007; Kelemen and Matter, 2008]. Carbonation in forsterite

31 involves the dissolution of olivine by hydrogen ions in solution,

32 $$Mg_2SiO_4 + 4H^+ \rightarrow 2Mg^{2+} + SiO_2(aq) + 2H_2O \qquad (1)$$
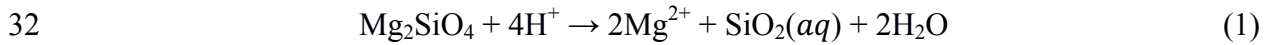
33 followed by the precipitation of magnesite ($MgCO_3$) via reaction between magnesium and

34 carbonate ions in solution:

35 $$Mg_2+ + CO_3^{2-} \rightarrow MgCO_3 \qquad (2)$$

36 Other precipitation reactions are also possible, including formation of brucite (magnesium

37 hydroxide) and serpentine minerals. Because the magnesium silicate is far from equilibrium with

38 CO_2-rich fluids, aqueous mineral carbonation of olivine is one of the kinetically fastest carbonation

39 reactions [Kelemen and Matter, 2008; Andreani et al, 2009]. The efficiency of carbon

40 sequestration methods is mainly determined by the supply of reactive fluids and exposure of

41 reactive solids to the CO_2-rich fluids [e.g., O'Connor et al., 2004]. The usefulness of ultramafic

42 rocks as carbon storage thus hinges on the feasibility of creating and maintaining reactive surface

43 area. Current implementation strategy includes grinding of solid reactants in *ex-situ* mineral

44 carbonation reactors [e.g., Gerdemann et al., 2007; Lackner et al., 1995], hydrofracturing of the

45 formations through *in-situ* deposition in ultramafic mines [Harrison et al., 2013; Power et al., 2013]

46 or injection of CO_2 in basalts [Matter et al., 2016]. These processes are energy intensive and costly

47 [Gerdemann et al., 2007; IPCC, 2005].

48   The hydration and carbonation of olivine results in an up to ~44% increase in solid molar

49 volume [e.g., Kelemen and Matter, 2008]. The conventional wisdom is that unless the reaction

50 products are deposited elsewhere, excess solids can clog fluid pathways and reduce the accessible

51 reactive surface, causing negative feedback to halt further reaction. However, field observations

52 show 100% serpentinization and carbonation of peridotite [e.g., Macdonald and Fyfe, 1985; Iyer

53 et al., 2008; Beinlinch et al., 2012] even when the alteration is nearly isochemical [Kelemen and

54 Matter, 2008]. The field data lead to a working hypothesis that excess solid reaction products could

55 exert enough pressure (termed crystallization pressure) to break the host rocks [O'Hanley, 1992;

56 Kelemen and Hirth, 2012]. This so-called reaction-driven cracking can create additional fluid

57 pathways and expose new reactive surface. When reaction-driven cracking is assumed, numerical

58 models show that olivine carbonation can proceed to completion at reasonable rates [e.g., Rudge

59 et al., 2010]. Because natural rocks are often subjected to complex mechanical, chemical, and

60   thermal loads, it is unclear at what conditions these solid volume increasing reactions can proceed

61   to completion.

62   Fracturing rocks via crystallization pressure is observed in salt weathering, where the salt

63   derives from external sources [Scherer, 2004; Noiriel et al., 2010]. At reservoir conditions,

64   however, the slow precipitation of magnesium carbonate (eqn. 2) is coupled with the rapid

65   dissolution of olivine (eqn. 1) [Chen et al., 2006; Xu et al., 2013; Johnson et al., 2014]. The

66   asymmetry in dissolution-precipitation kinetics renders it difficult to generate large crystallization

67   pressure. Indeed, experimental studies of CO_2-rich brine reacting with peridotites have not

68   produced evidence for cracking via crystallization pressure in olivine [e.g., Hovelmann et al.,

69   2012]. Instead, laboratory studies consistently show that rates of carbonation and hydration

70   decrease with time [O'connor et al., 2004; Andreani et al., 2009; Hovelmann et al., 2012].

71   Whether fracturing the solid reactants is achievable without additional energy input

72   remains a critical question. We report on insights gained during an *in-situ* synchrotron-based X-

73   ray microtomography (SXμT) experiment that characterized the real-time evolution of 3-

74   dimensional (3D) pore geometry during olivine carbonation and highlight an alternative

75   mechanism that might facilitate natural carbonation reactions.

76   **Data Collection and Reduction**

77   A sintered porous olivine aggregate was chosen to react with a sodium bicarbonate solution

78   ($NaHCO_3$, 1.5 mol) at a confining pressure of 13 MPa, a pore fluid pressure of 10 MPa and a

79   temperature of $200^{o}C$ (Supporting Information fig. S1). We utilized an x-ray transparent version

80   of a Hassler core holder [Fusseis et al., 2014] to investigate the 3D microstructure evolution during

81   olivine carbonation. The core holder was installed in a SXμT beamline at the Advanced Photon

82   Source, where the change of rock's microstructure was recorded.

83   From the moment when the temperature at the sample reached 200°C, every 30 minutes

84   1500 projections were collected with an exposure time of 50 ms while the sample was rotated over

85   180° with 1.2 $°s^{-1}$. Between 128 and 135 hours, data were acquired in 5-minute intervals. Each

86   dataset was acquired in 150 s. A total of 360 3D datasets amounting to 35 TB of raw data cover

87   the entire experiment. From the radiographic projection data, 3D SXμT data with a spatial

88   resolution of ~2 μm were reconstructed using a single-distance phase retrieval algorithm

89   implemented in TomoPy [Paganin et al., 2002; Gürsoy et al., 2014].

90   After the reacted olivine sample was retrieved, Synchrotron-based X-ray nanotomography
91   data were collected from a 65x65x63 μm^3 fragment of the post-reaction olivine aggregate, using a
92   transmission X-ray microscope at beam line 32-ID of APS [Paganin et al., 2002]. The instrument
93   uses an 8 keV monochromatic beam and an X-ray objective lens to magnify radiographs onto a
94   detection system assembly comprising a scintillator (LuAG single crystal scintillator), a Zeiss 5X
95   optical microscope objective lens and an Andor Neo sCMOS camera. The Fresnel zone plate limits
96   the spatial resolution to 60 nm, while the voxel size is 57 nm after binning. A total of 720 projection
97   images were acquired over a 180° rotation angle range (i.e., in 0.25° angular steps) with 2s
98   exposure time for each image.

99   Because of the weak x-ray absorption contrast between magnesite and olivine at 8 keV, an
100   iterative reconstruction method, penalized maximum-likelihood (PML) [De Carlo et al., 2014] is
101   integrated in Tomopy [Chang et al., 2004; Gürsoy et al., 2014] to enhance the signal to noise ratio.
102   This algorithm is proven to produce high quality reconstructions, especially for tomograms with
103   noisy radiographs and sampling below the Nyquist criterion [De Andrade et al., 2016]. The
104   reconstruction of a full volume with such high computational requirements method necessitates
105   the use of a supercomputer at the Argonne Leadership Computing Facility (ALCF), where a new
106   large-scale parallelization approach has been implemented [Biçer et al., 2015].

107   For geochemical analyses of the post-reaction sample, the retrieved fragments were
108   embedded in epoxy and exposed in a polished surface. Mineral phases were identified with
109   energy-dispersive x-ray spectroscopy in a JEOL JXA-8900 Electron probe microanalyzer
110   operating at a 15 keV accelerating voltage and a beam current of 15 nA. Collection time for EDS
111   data was 120 s per spot.

112   The reconstructed data were visualized and analyzed using the commercial software Avizo
113   Fire. No image processing other than cropping was applied. To determine the threshold value, grey
114   value histograms (Supporting Information, figs. S2) were computed from all analyzed time steps,
115   smoothed, and the individual distributions superposed, following an approach described in
116   [Fusseis et al., 2012]. The gray value distribution in each dataset is a direct function of the sample
117   composition and changes during the reaction. Since porosity is produced, the proportion of dark
118   voxels increases systematically at the expense of the intermediate grey voxels, causing the
119   individual lines to intersect in a narrow region. The gray value at which the lines intersect was
120   used for thresholding. An increase in the brightest voxels, which can also be seen in the histograms,

121   is a consequence of phase contrast around newly produced pores (Supporting Information, figs.

122   S3).

123   **Results**

124   The SXμT time-series data provide clear evidence that the carbonation reaction progressed

125   steadily while volume expansion and fracturing of the olivine aggregate took place as a result of

126   olivine carbonation (Figs. 1, 2). Fine-grained reaction products precipitated in the interior of the

127   cup wall and appear as growing clusters with smoother textures and less contrast (magenta outlines

128   in Fig. 1). The sizes of the clusters increase with time. Nanotomography and energy-dispersive

129   spectroscopy confirm that the precipitate clusters are formed by new carbon-rich minerals, likely

130   magnesite (Fig. 3). Changes in the position of individual olivine grains (yellow arrows in Figs. 1,

131   2), which act as strain markers, are evidence for the volume expansion caused by the reaction.

132   Outlined by the surrounding pores, the precipitation clusters become more discernible in

133   the tangential sections underneath the outer cup surface (Figs. 2A-E). A polygonal crack system

134   emerges after 84 hours (Fig. 2C). In Fig. 1, it becomes apparent that the integrity of the cup wall

135   is deteriorated by these cracks, which propagate into the cup wall from about 64 hours into the

136   experiment. Fractures are seen to form at both the inner and outer surfaces of the cup wall (Fig. 1),

137   and then propagate towards the interior as carbonation continues (Supporting Information, movie

138   M1). These cracks widen to several tens of μm as reaction continues (Fig. 1) and eventually

139   disintegrate the cup, as a post-mortem examination of the sample revealed.

140   Simultaneously, the total porosity evolves in the sintered cup wall (Fig. 4). The total

141   porosity, which is normalized to the starting porosity, increases by a factor of 1.2 in both

142   subvolumes v1 and v2 during the first 90 hours of reaction. After that, the porosity of v1 continues

143   to increase to a factor of 1.3 until ~100 hours, when it starts a steady decline. In contrast, the

144   porosity of v2 remains at just above 1.2, with only minor declines followed by recovery. (Fig. 4B).

145   We evaluated the porosity distribution within the two subvolumes by means of quantifying

146   porosity on 2-dimensional (2D) tangential sections extracted from the segmented subvolumes

147   along the radius of the sample (Figs. 4C&D, Supplementray Information fig. S4). At the early

148   stages of the reaction (i.e., < 90 hours), porosity of all the tangential sections increases, likely due

149   to dissolution of olivine grains (Figs. 4C&D). After that, porosity of the interior tangential sections

150   decreases monotonically, consistent with the appearance of precipitants (Figs. 1, 2). In contrast,

151   the porosity of the 2D sections near the (inner) surface of v1 continues to increase after 90 hours

152   (Fig. 4C). The sections near the (outer) surface of v2 exhibits similar porosity increases (Fig. 4D).

153   The contrast between the porosity decreasing interior and the porosity increasing surfaces indicates

154   that more reaction products are precipitated in the interior of the cup wall (cf. Fig. 1). This non-

155   uniform precipitation corroborates with the observed total porosity changes in v1 and v2: the total

156   porosity in v1 with more pores from the interior regions decreases, whereas the total porosity of

157   v2 with less interior regions remains constant (Fig. 4B).

158   The carbonation reaction also constantly modifies the surface roughness of the olivine

159   grains inside the cup. The rhombohedral shape of the new crystals on the surface of the olivine

160   sand grains suggests that they are magnesite $MgCO_3$ (Fig. 5A). Both the population and size of

161   these magnesite grains increase steadily during the entire experiment (Fig. 5B), with no indication

162   of self-limiting behavior.

163   **Discussion**

164   Our experiment elucidates the real-time evolution of 3D microstructure during olivine

165   carbonation, provides insight into the processes controlling the metamorphic reaction. Our data

166   reveal a positive feedback between reaction progress and porosity evolution. Of particular

167   importance is the polygonal crack pattern initiated on the surfaces of the cup wall (Figs. 1, 2).

168   Growth of these cracks helps maintain reactive surfaces, and eventually leads to the disintegration

169   of the sample (Supporting Information, movie M1).

170   Polygonal crack patterns are frequently observed in drying mud ponds [Goehring et al.,

171   2010], cooling lava flows [Aydin and DeGraff, 1988], and ice wedge fields [Plug and Werner,

172   2002; Kessler and Werner, 2003] Formation of polygonal cracks requires volume mismatch

173   between the surface and the interior of the material, which leads to a stress buildup in the surface

174   layer [Shorling et al., 2000]. When the stress exceeds the tensile strength, cracks develop in the

175   surface layer. Cracking at the surface results in accelerated water loss (in desiccating mud), heat

176   loss (in cooling lava), or thermal contraction (in ice wedge) from the interior of the material.

177   Consequently, the cracks propagate into the interior of the material. We infer these processes to

178   have also controlled reaction advance in our experiment and may affect natural carbonation.

179   In our experiment, reaction advance is strongly affected by the sample geometry (Fig. 6).

180   Dissolution of olivine in the cup wall is expected to be vigorous because smaller crystals dissolve

6

181 more rapidly [Adamson, 1990; Emmanuel and Ague, 2009]. The surge in magnesium ions in

182 solution promotes precipitation of new crystals (Figs. 1-3). At the wall's interior, precipitation

183 causes the infill of the pore space and solid volume expansion (Fig. 6). At the surfaces, however,

184 the fine olivine grains in the cup wall are adjacent to the olivine sand grains, both the ones filled

185 inside the cup as well as the ones spilled to its outside. These sand grains are ~2 orders of

186 magnitude larger than the grains in the cup wall. Since crystallization rate negatively correlates

187 with the curvature of the substrate [Garcia et al., 2013; Ziese et al., 2013], precipitation of new

188 crystals preferentially takes place on the large olivine sand grains at the expense of the neighboring

189 fine grains (Fig. 6). The lack of precipitation at the surfaces of in the cup wall is confirmed by

190 porosity measurements (Fig. 4). The non-uniform precipitation causes the interior of the cup wall

191 to expand faster than its surfaces, thus generating the tensile stresses necessary for cracking to

192 occur at the surfaces (Fig. 6). The polygonal patterns (Fig. 2) suggest that the cracks are generated

193 by the same mechanism as for the shrinkage cracks [e.g., Shorlin et al., 2000]. In our experiment,

194 the volume mismatch between the surface and interior of the sintered olivine aggregate is

195 instigated by rapid dissolution and non-uniform precipitation. In contrast to the crystallization

196 pressure hypothesis, the mechanism proposed here is based on the mismatch between the volume

197 changes in different parts of the sample and can tear the surface for tension values less than the

198 confining pressure. Coalescence of the polygonal cracks leads to fractures disintegrating the

199 cylindrical samples. Because of the cylindrical geometry of the samples, radial expansion is

200 counteracted by the hoop stress it would generate. Due to this effect and the different loading

201 systems in the axial and radial directions, the axial stress on the sample is the least compressive

202 and the largest fractures are horizontal (Fig. 2).

203   In homogeneous materials, the primary shrinkage cracks intersect at right angles because

204 the first set of cracks releases the stress normal to their surface, and consequently the second set

205 of cracks forms perpendicular to the preexisting first set to alleviate stress in that direction [e.g.,

206 Goehring et al, 2010]. The geometric attribute can be used to verify the cracking mechanism during

207 olivine carbonation in our experiment. Indeed, the nanotomography data of the post-reaction cup

208 wall reveal nanometer scale cracks intersecting each other orthogonally (Supporting Information,

209 movie M2), in good agreements with the predicted right angle of the primary cracks formed in a

210 layer under tension [e.g., Goehring et al, 2010].

Conclusion

The time-resolved microtomography study reveals an experimentally tested mechanism for self-sustained olivine carbonation. The mechanism is the similar to that in the shrinkage cracking observed in other geological settings, though during olivine carbonation, it is the volume expansion of the interior, instead of the contraction of the surface, that causes the volume-mismatch between the surface and the interior. Compared to the crystallization pressure hypothesis, the polygonal pattern associated with tensile cracking at the surface is more consistent with fracture patterns observed in rocks that undergo natural weathering [e.g., Iyer et al., 2008]. Understanding the mechanism of reaction-induced cracking can lead to new implementation strategy of more efficient carbonation reactors. Although our experiment was conducted on porous aggregates at reservoir conditions, it is possible that cracking by the same mechanism takes place in other geological settings. In nature, carbonation of mantle peridotite can start with a pre-existing fracture network, and proceed to completion with reaction-induced cracking, as long as the non-uniform volume expansion is maintained.

References

Adamson, A.W., Physical Chemistry of Surfaces, 5th ed., Wiley, New York, 1990.

Andreani M., Luquot L., Gouze P., Godard M., Hoise E., Gibert B.: Experimental study of carbon sequestration reactions controlled by the percolation of CO2-rich brine through peridotites. Environ. Sci. Technol. 43, 1226–1231, 2009.

Aydin, A., DeGraff J.M., Evolution of polygonal fracture patterns in lava flows. Science 239, 471–476, 1988.

Beinlich A., Plümper O., Hövelmann J., Austrheim H., Jamtveit B., Massive serpentinite carbonation at Linnajavri, N–Norway. Terra Nova 24, 446-455, 2012.

Biçer, T., et al., Rapid tomographic image reconstruction via large-scale parallelization. Lecture Notes in Computer Science, 9233, 289–302, 2015.

Chang, J-H, Anderson, JMM, Votaw J.T., Regularized image reconstruction algorithms for positron emission tomography. Medical Imaging, IEEE Transactions on 23(9), 1165–1175, 2004.

239 Chen Z.Y., O'Connor W. K., Gerdemann S. J., Chemistry of aqueous mineral carbonation for
240   carbon sequestration and explanation of experimental results. Environ. Prog. 25, 161–166,
241   2006.

242 De Andrade, V., Deriy, A., Wojcik, M. J., Gürsoy, D., Shu, D., Fezzaa, K., & De Carlo, F.,
243   Nanoscale 3D imaging at the Advanced Photon Source. SPIE Newsroom.
244   doi:10.1117/2.1201604.006461, 2016.

245 De Carlo, F., et al., Scientific data exchange: a schema for hdf5-based storage of raw and analyzed
246   data. Journal of Synchrotron Radiation 21(6), 1224–1230, 2014.

247 Emmanuel, S., Ague J.J., Modeling the impact of nano-pores on mineralization in sedimentary
248   rocks. Water Resour. Res. 45, W04406, doi:10.1029/2008WR007170, 2009.

249 Fusseis F., et al., A low-cost X-ray transparent experimental cell for Synchrotron-based X-ray
250   microtomography studies at geological reservoir conditions. J. Synch. Rad. 21, 251-253,
251   2014.

252 Fusseis, F., et al., Pore formation during dehydration of a polycrystalline gypsum sample observed
253   and quantified in a time-series synchrotron X-ray micro-tomography experiment, Solid Earth,
254   3, 71-86, 2012.

255 García N.A., Register R.A., Vega D.A., Gómez L. R., Crystallization dynamics on curved surfaces.
256   Phys. Rev. E 88, 012306, 2013.

257 Gerdemann S.J., O'Connor W.K., Dahlin D.C., Penner L.R., Rush H., Ex-situ Aqueous Mineral
258   Carbonation. Environ. Sci. Technol. 41, 2587–2593, 2007.

259 Giammar D.E., Bruant R.G., Peters C.A., Forsterite dissolution and magnesite precipitation at
260   conditions relevant for deep saline aquifer storage and sequestration of carbon dioxide. Chem.
261   Geol. 217, 257-276, 2005.

262 Goehring L., Conroy R., Akhter A., Clegg W.J., Routh A.F., Evolution of mud-crack patterns
263   during repeated drying cycles. Soft Matter 6, 3562–3567, 2010.

264 Goff F., Lackner, K.S., Carbon dioxide sequestering using ultramafic rocks. Environ. Geosci. 5,
265   89-101, 1998.

266 Gürsoy D., De Carlo F., Xiao X., Jacobsen C., TomoPy: a framework for the analysis of
267   synchrotron tomographic data. J. Synchrotron Rad. 21(5), 1188-1193, doi:
268   10.1107/S1600577514013939, 2014.

269 Guyot F., Daval D., Dupraz S., Martinez I., Menez B., Sissmann O., CO2 geological storage: the
270   environmental mineralogy perspective. Compte Rendu Geosci. 343, 246–259, 2011.

271 Harrison A.L., Power I.M., Dipple G.M., Accelerated carbonation of brucite in mine tailings for
272   carbon sequestration. Environ. Sci. Technol. 47, 126-134, 2013.

273 Hovelmann J., Austrheim H., Jamtveit B., Microstructure and porosity evolution during
274   experimental carbonation of a natural peridotite. Chem. Geol. 334, 45-265, 2012.

275 IPCC, IPCC Special Report On Carbon Dioxide Capture And Storage. Cambridge University
276   Press, Cambridge UK and New York USA, 2005.

277 Iyer K., Jamtveit B., Mathiesen J., Malthe-Sorenssen A., Feder J, Reaction-assisted hierarchical
278   fracturing during serpentinization. Earth Planet Sci Lett 267, 503-516, 2008.

279 Johnson N.C., Thomas, B., Maher, K., Rosenbauer, R. J., Bird, D., & Brown, G. E., Olivine
280   dissolution and carbonation under conditions relevant for in situ carbon storage. Chem. Geol.,
281   373, 93–105, 2014.

282 Kelemen K.B., Hirth G., Reaction-driven cracking during retrograde metamorphism: Olivine
283   hydration and carbonation. Earth Planet. Sci. Lett. 345, 81-89, 2012.

284 Kelemen P., Matter, J.M., In situ carbonation of peridotite for CO2 storage. Proc. Nat. Acad. Sci.
285   105, 17295-300, 2008.

286 Kessler M.A., Werner B.T., Self-organization of sorted patterned ground. Science 299, 380-383,
287   doi:10.1126/science.1077309, 2003.

288 Lackner, K.S., Climate Change: A Guide to CO2 Sequestration. Science 300, 1677-1678, 2003.

289 Lackner K.S., Wendt C.H., Butt D.P., Joyce E.L., Sharp D.H., Carbon dioxide disposal in
290   carbonate minerals. Energy 20, 1153-1170, 1995.

291 Macdonald A.H., Fyfe W.S., Rate of serpentinization in seafloor environments. Tectonophysics
292   116, 123-135, 1985.

293 Matter, J.M. et al., Rapid carbon mineralization for permanent disposal of anthropogenic carbon
294   dioxide emissions. *Science*. 352, doi: 10.1126/science.aad8132, 2016.

295 Noiriel C., Renard F., Marie P.L., Doan M.L. Gratier J.P., Intense fracturing and fracture sealing
296   induced by mineral growth in porous rocks. Chem. Geol. 269(3-4), 197- 209, doi:
297   10.1016/j.chemgeo.2009.09.018, 2010.

298 O'Connor W.K., Dahlin, D.C., Rush, G.E., Gerdemann, S.J., Penner, L.R., and Nilsen, D.N.,
299   Aqueous mineral carbonation: mineral availability, pretreatment, reaction parameters, and
300   process studies. DOE/ARC-TR-04-002, 2004.

301 O'Hanley D.S., Solution to the volume problem in serpentinization. Geology, 20, 705-708, 1992.

302 Paganin, D., Mayo, S.C., Gureyev, T.E., Miller, P.R. and Wilkins, S.W., Simultaneous phase and
303   amplitude extraction from a single defocused image of a homogeneous object, Journal of
304   Microscopy, 206, 33-40, 2002.

305 Plug L.J., Werner B.T., Nonlinear dynamics of ice-wedge networks and resulting sensitivity to
306   severe cooling events. Nature 417, 929–933, 2002.

307 Power, I.M. Harrison, A., Dipple, G., Wilson, S., Kelemen, P., Hitch, M., Southam, G., Carbon
308   mineralization: from natural analogues to engineered systems. Reviews in Mineralogy and
309   Geochemistry 77, 305-360, 2013.

310 Rudge J.F., Kelemen K.B., Spiegelman M., A simple model of reaction-induced cracking applied
311   to serpentinization and carbonation of peridotite. Earth Planet. Sci. Lett. 291, 215-221, 2010.

312 Seifritz, W., CO2 disposal by means of silicates. Nature 345, 486-486, 1990.

313 Scherer G. W., Stress from crystallization of salt. Cement and Concrete Research, 34(9), 1613–
314   1624. doi:10.1016/j.cemconres.2003.12.034, 2004.

315 Shorlin K.A., de Bruyn J.R., Graham M., Morris S.W., Development and geometry of isotropic
316   and directional shrinkage crack patterns. Phys. Rev. E. 61, 6950–6957, 2000.

317 Xu J., Yan C., Zhang F., Konishi H., Xu H., Teng H., Testing the cation-hydration effect on the
318   crystallization of Ca–Mg–CO3 systems. Proc Natl Acad Sci USA 110(44), 17750-17755,
319   2013.

320 Ziese F., Maret G., Gasser U., Heterogeneous nucleation and crystal growth on curved surfaces
321   observed by real-space imaging. J. Phys.: Condens. Matter 25: 375105, doi:10.1088/0953-
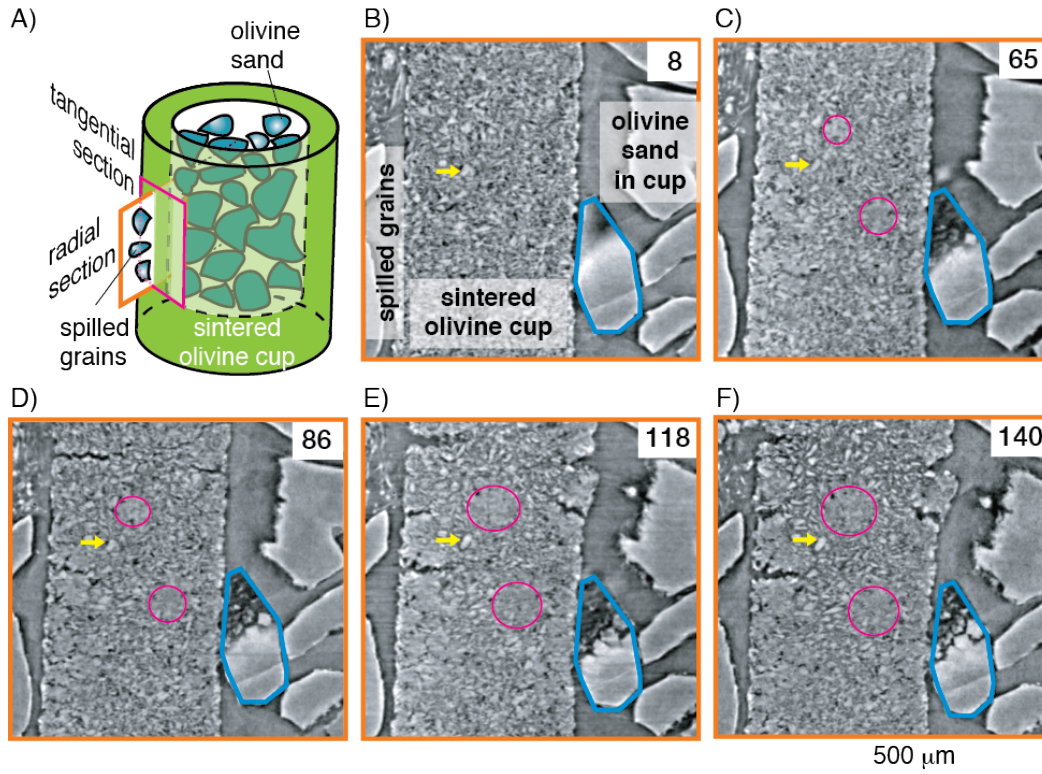322   8984/25/37/375105, 2013.

11

Figure 1. Temporal evolution of pore geometry in a radial section. A) A thick-walled cup (made of a sintered olivine aggregate) filled with olivine sand. Microtomographic image of a radial section (orange outline) after B) 8; C) 65; D) 86; E) 118; F) 140 hours of carbonation. Yellow arrows mark an olivine grain in the interior of the cup wall. Olivine sand grains in the cup (right side of the images) show considerable increase in surface roughness. Time series images of the surface of a representative olivine sand grain (blue outline) are presented in Figure 5. Some olivine sand grains fell between the olivine cup and the jacket during sample preparation (spilled grains on the left side of the images). Fine-grained reaction products precipitated in the interior of the cup wall appear as growing clusters with smoother textures (magenta outline). Cracks initiate at both the inner and outer surfaces of the cup wall after 64 hours of reaction. Cracks widen as reaction continues.

349
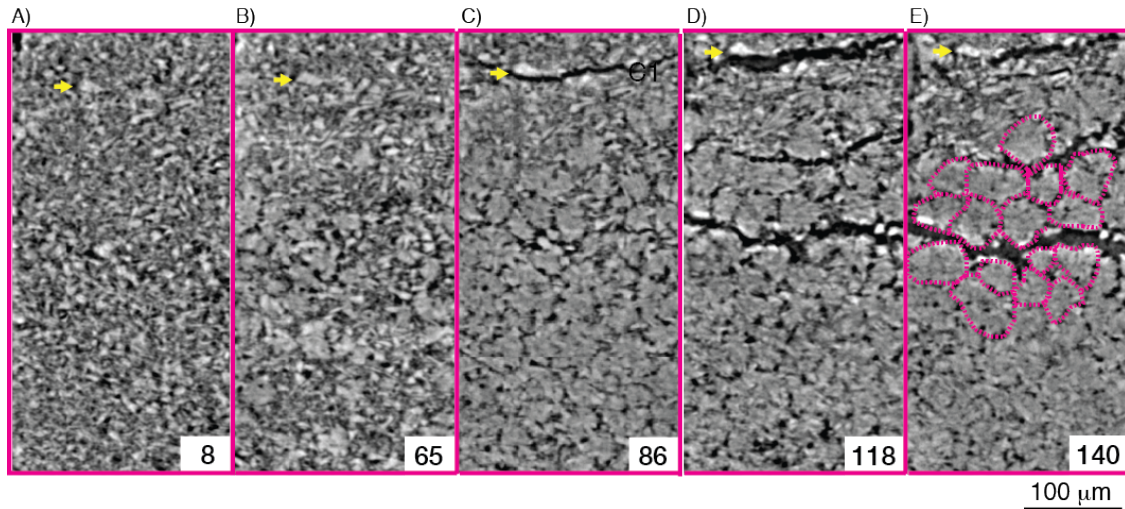
Figure 2. Temporal evolution of pore geometry in a tangential section. Microtomographic image of a tangential section of the olivine cup (magenta outline in Fig. 1A) undergoing A) 8; B) 65; C) 86; D) 118; E) 140 hours of carbonation. Yellow arrows mark an olivine grain in the interior of the cup wall. Its position change with respect to the top of the image window (fixed) serves as a strain marker for the volume expansion resulting from reactions. In the tangential section, polygonal cracks develop along the edge of the reactant clusters (magenta outline). Coalescence of the polygonal cracks leads to fractures across the aggregate.

357


358
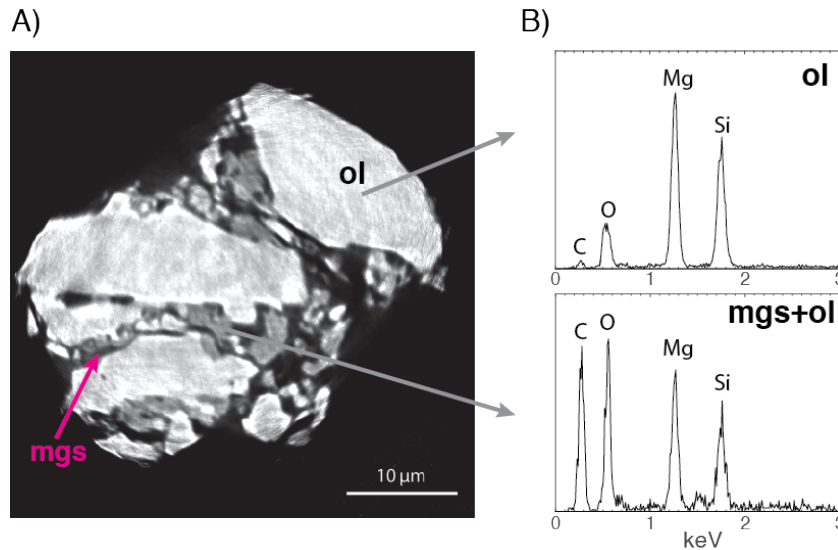
Figure 3. Segment of the post-reaction cup wall. A) A 2D nanotomographic image shows that new phases (mgs, dark grey) precipitate in the pore space between olivine grains (ol, light grey) of the olivine aggregate; B) EDS data of the post-reaction cup wall. The weak carbon signal in the spectrum of olivine grains results from carbon coating. In contrast, the spectrum of the regions filled with precipitants (mgs+ol) shows significant carbon content, which suggests epitaxial magnesite (mgs) growth on the olivine grains (ol).

14

365
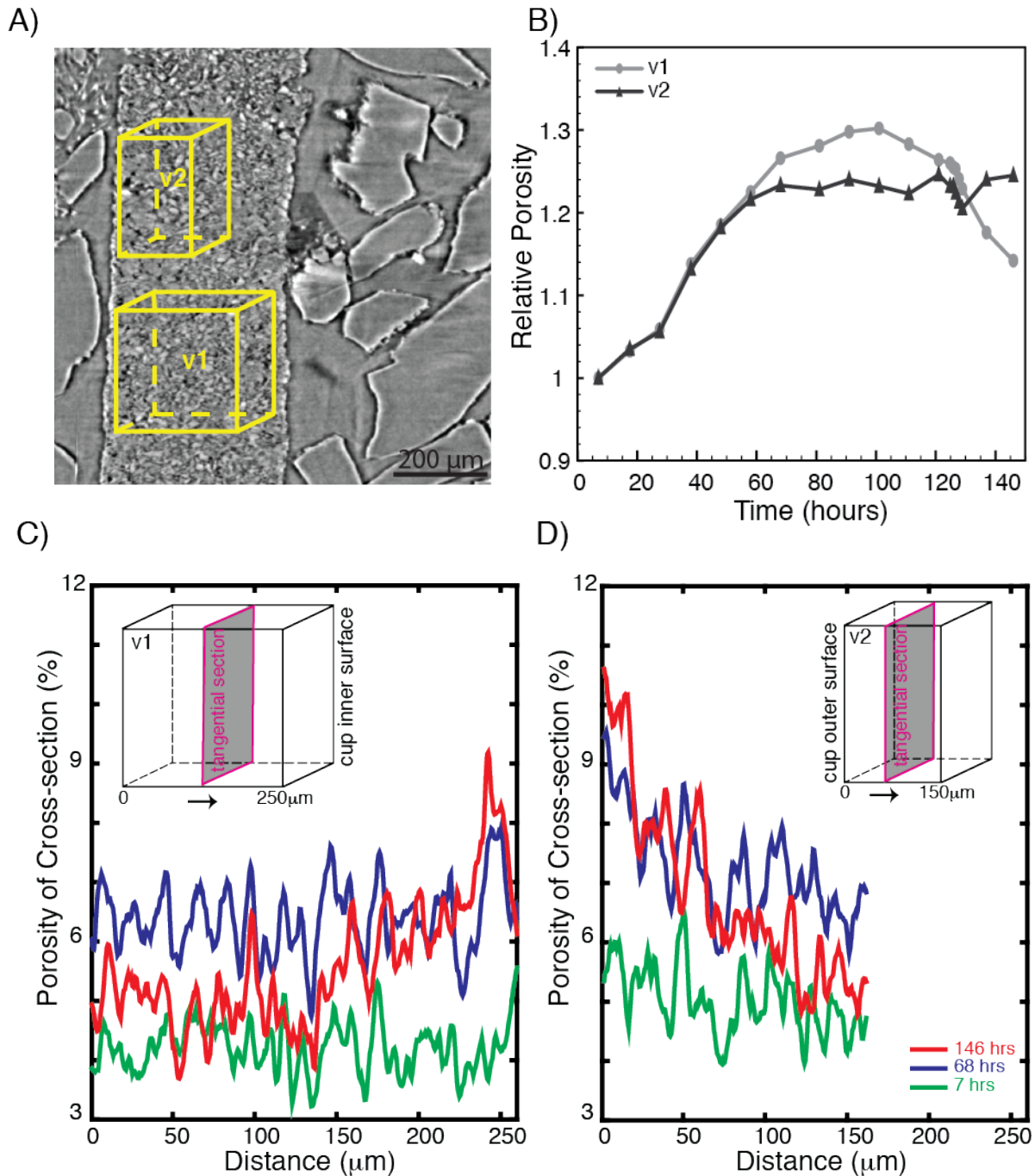
Figure 4. Porosity evolution of subvolumes. A) Subvolumes v1 and v2; B) Relative porosity change of v1 (light grey) and v2 (dark grey) during 146 hours of olivine carbonation. C) Porosity evolution of 2D tangential sections (magenta slice) taken from C) subvolume v1; D) subvolume v2 after 7 (green), 68 (blue), 146 (red) hours of reactions. Note that the leftmost edge of subvolume 2 is at the outer surface of the olivine cup wall, the rightmost edge of subvolume 1 is at the inner surface of the cup wall. Porosity at the interior first increases and then decreases during carbonation, whereas porosity near both the outer and inner surfaces increases.
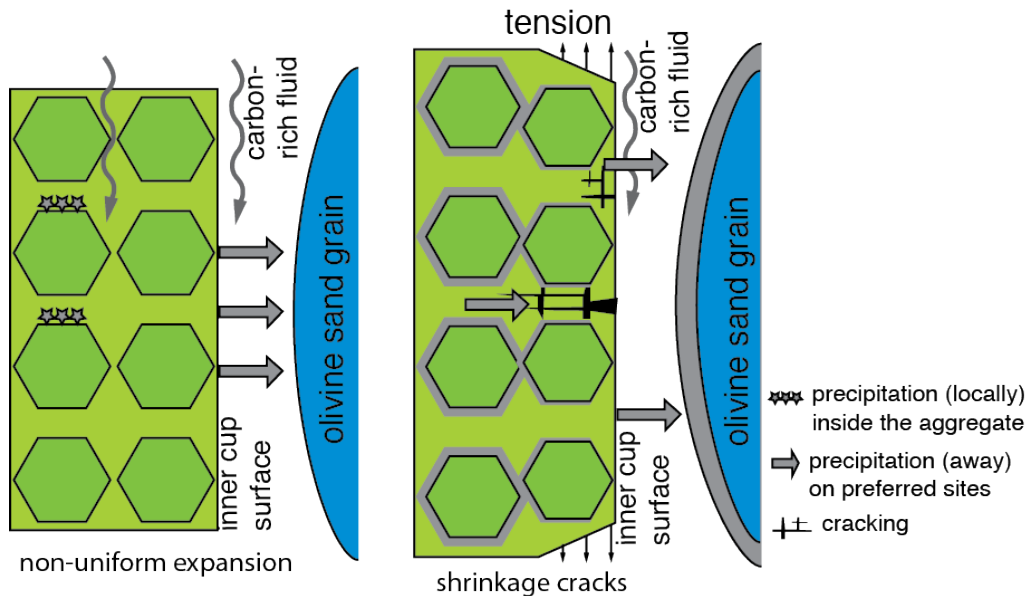
15

373

374
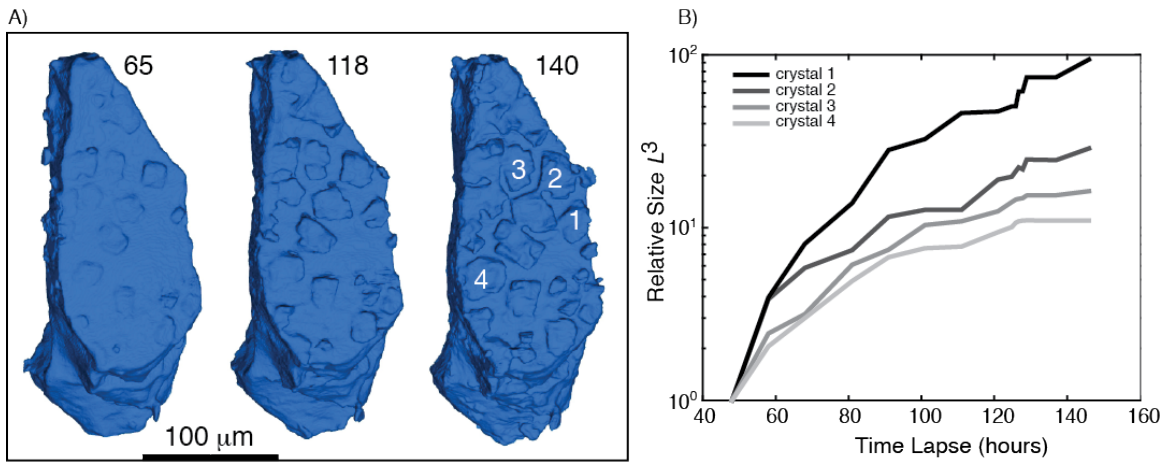
Figure 5. Nucleation and growth of new crystals. A) Surface of a representative olivine sand grain
(blue outline in Fig. 1) in the olivine cup; B) Cubic circumferential length L (normalized to that at
48 hours of carbonation when most of the new crystals first appeared) of several new crystals as a
function of time.

379

380

Figure 6. Schematic diagram for shrinkage cracking during mineral carbonation. At the surface of
the fine-grained olivine aggregate (green), reactants (grey) preferentially precipitate on the large
olivine sand grains (blue). Beneath the surface of the cup wall, reactants precipitate locally (grey
stars), leading to non-uniform volume expansion. As the reaction continues, cracks form in
response to increasing strain.

386